Research Square

Preprints are preliminary reports that have not undergone peer review.
They should not be considered conclusive, used to inform clinical practice,
or referenced by the media as validated information.

PARG inhibition eliminates base excision repair-deficient and non-proliferating cancer cells through toxic PAR accumulation

Erina Kusakabe
Ehime University
Masahiro Matsuki
Alivexis, Inc
Takeo Urakami
Alivexis, Inc
Takafumi Shimizu
Alivexis, Inc
Taisuke Takahashi
Alivexis, Inc
Ryo Kamata
Ehime University
Sota Tate
Ehime University
Shiho Nakano
Ehime University
Shojiro Kitajima
Keio University
Hiroyuki Sasanuma
Tokyo Metropolitan Institute of Medical Science
Koji Hirota
Tokyo Metropolitan University
Yoshiaki Kamei
Ehime University
Yuzo Umeda
Ehime University
Yoh Terada
Alivexis, Inc
Junko Murai
murai.junko.nk@ehime-u.ac.jp

Ehime University

Research Article

Keywords: PARG, parthanatos, replica*on stress, poly(ADP-ribose)ylation, base excision repair, mitochondria dysfunction

Posted Date: July 8th, 2026

DOI: https://doi.org/10.21203/rs.3.rs-10223032/v1

License: This work is licensed under a Creative Commons Attribution 4.0 International License.
Read Full License

Additional Declarations:
Competing interest reported. J. Murai receives a research fund from Alivexis, Inc.. Y. Terada is a full-time board director of Alivexis, Inc. and holds stock options in the company. M. Matsuki is a full-time employee of Alivexis, Inc. and holds stock options in the company. T. Shimizu is a full-time employee of Alivexis, Inc. and holds stock options in the company. T. Takahashi is a full-time employee of Alivexis, Inc. and holds stock options in the company. T. Urakami is a full-time employee of EVerMed, Inc. and holds stock options in Alivexis, Inc.

Procedures involving the care and use of animals in this study were reviewed and approved by the Institutional Animal Care and Use Committee of Jubilant Biosys Ltd. prior to the initiation of this study. Animal care and experimental procedures were conducted in accordance with the principles outlined in the Guide for the Care and Use of Laboratory Animals, 8th Edition (National Research Council, 2011).

Title

PARG inhibition eliminates base excision repair-deficient and non-proliferating cancer cells through toxic PAR accumulation

Authors information

Erina Kusakabe[1,2], Masahiro Matsuki[3], Takeo Urakami[3,*], Takafumi Shimizu[3], Taisuke Takahashi[3], Ryo Kamata[1,4], Sota Tate[1,4], Shiho Nakano[1], Shojiro Kitajima[5], Hiroyuki Sasanuma[6], Koji Hirota[7], Yoshiaki Kamei[2], Yuzo Umeda[2], Yoh Terada[3, #], Junko Murai[1,4, #]

[1]Department of Biochemistry and Molecular Genetics, Graduate School of Medicine, Ehime University, Toon, Ehime, 791-0295, Japan

[2]Department of Hepato-Biliary-Pancreatic Surgery and Breast Surgery, Graduate School of Medicine, Ehime University, Toon, Ehime, 791-0295, Japan

[3]Alivexis, Inc., Tokyo, Japan.

[4] Department of Cell Growth and Tumor Regulation, Proteo-Science Center, Premier Institute for Advanced Studies, Ehime University, Toon, Ehime, 791-0295, Japan

[5] Institute for Advanced Biosciences, Keio University, Tsuruoka, Yamagata, 997-0017, Japan

[6] Department of Genome Dynamics, Tokyo Metropolitan Institute of Medical Science, Tokyo, 156-8506, Japan

[7]Department of Chemistry, Graduate School of Science, Tokyo Metropolitan University, Hachioji, Tokyo 192-0397, Japan

[#]Corresponding authors

Junko Murai: murai.junko.nk@ehime-u.ac.jp

ORCID: 0000-0003-2023-6160

Yoh Terada: terada@alivexis.com

[*]Present address: EVerMed, Inc., Tokyo, Japan

Abstract

Poly(ADP-ribose) glycohydrolase (PARG) is the primary enzyme responsible for degrading poly(ADP-ribose) (PAR) chains generated by poly(ADP-ribose) polymerases (PARPs) during DNA damage responses. Although pharmacological inhibition of PARG has emerged as a promising anticancer strategy targeting PAR metabolism, its cytotoxic mechanisms and the tumor contexts most susceptible to PARG inhibition remain incompletely understood. Here, we developed the novel PARG inhibitors, MOD000568 and MOD000582, and demonstrated their antitumor efficacy and tolerability in mouse xenograft models. Through an siRNA screen and biological experiments using genetically modified cells, we found that cellular vulnerability to PARG inhibition is strongly associated with elevated PAR metabolism, particularly base excision repair (BER) deficiency. Mechanistically, PARG inhibitors induced progressive accumulation of PARylated proteins, accompanied by nuclear translocation of apoptosis-inducing factor, a hallmark of parthanatos, caspase-dependent apoptosis, and mitochondrial dysfunction, while intracellular NAD^+ depletion was not the primary determinant of cell death. Importantly, PARG inhibitor–induced cytotoxicity occurred largely independently of DNA replication and extended to G1-arrested and senescence-like cells. Although BER deficiency enhanced sensitivity, genetic defects were not required, indicating that both BER deficiency and PAR-inducing stresses increase susceptibility by elevating PAR metabolism. These findings support a model in which PAR accumulation beyond a critical threshold determines cell fate and identify PARG inhibition as a therapeutic strategy for tumors with elevated PAR metabolism, including non-proliferating and therapy-resistant cell populations.

Keywords

PARG, parthanatos, replication stress, poly(ADP-ribose)ylation, base excision repair, mitochondria dysfunction

Statements and Declarations

J. Murai receives a research fund from Alivexis, Inc.. Y. Terada is a full-time board director of Alivexis, Inc. and holds stock options in the company. M. Matsuki is a full-time employee of Alivexis, Inc. and holds stock options in the company. T. Shimizu is a full-time employee of Alivexis, Inc. and holds stock options in the company. T. Takahashi is a full-time employee of Alivexis, Inc. and holds stock options in the company. T. Urakami is a full-time employee of EVerMed, Inc. and holds stock options in Alivexis, Inc.

Reachability (corresponding authors)

Full name: Junko Murai

Mailing address: 454 Shitsukawa, Toon, Ehime, 791-0295, Japan

Phone: +81-89-960-5254

Email address: murai.junko.nk@ehime-u.ac.jp

Full name: Yoh Terada

Mailing address: Daiichi Hibiya Building 7F, Shimbashi 1-18-21, Minato-ku, Tokyo 105-0004, Japan

Phone: +81 (0) 80-4930-7832

Email address: terada@alivexis.com

Introduction

Poly(ADP-ribose) polymerase 1 (PARP1) and PARP2 (hereafter collectively referred to as PARP unless otherwise indicated) are central components of the base excision repair (BER) pathway and are rapidly activated in response to DNA single-strand breaks (1). In cancer cells, endogenous stresses such as elevated reactive oxygen species, oncogene-induced DNA damage, or defects in DNA repair pathways can lead to sustained activation of PARP. PARylation is a highly dynamic post-translational modification whose abundance is tightly controlled by the opposing activities of PARP enzymes, which synthesize poly(ADP-ribose) (PAR), and poly(ADP-ribose) glycohydrolase (PARG), which hydrolyzes PAR chains (2). The balance between PAR synthesis and degradation therefore determines the extent and duration of PARylation in cells.

Therapeutic targeting of PAR metabolism has emerged as a successful strategy in oncology (3). PARP inhibitors impair repair of single-strand DNA lesions and promote the formation of DNA double-strand breaks, thereby inducing synthetic lethality in homologous recombination (HR)–deficient tumors through catalytic inhibition and PARP trapping (4-6), which has led to major clinical advances in breast, ovarian, prostate, and pancreatic cancers (7). In parallel, PARG inhibitors have been developed as an alternative strategy to disrupt PAR homeostasis (8). Preclinical studies have suggested that PARG inhibition preferentially affects cancer cells harboring defects in DNA replication stress response, BER, or HR (7-11). However, the mechanisms underlying PARG inhibitor-induced cytotoxicity remain incompletely understood, and robust biomarkers that predict sensitivity have not yet been established.

Parthanatos is a distinct form of programmed cell death triggered by excessive activation of PARP in response to severe DNA damage or other cellular stresses (9, 10). In classical parthanatos, rapid PAR synthesis is accompanied by NAD^+ and ATP depletion, accumulation of cytosolic PAR, release and nuclear translocation of apoptosis-inducing factor (AIF) from mitochondria (11), and large-scale DNA fragmentation and chromatin condensation in a largely caspase-independent manner. Although this pathway is well established under acute DNA damage conditions, several fundamental aspects remain unresolved (12), including the relative contribution of NAD^+ depletion, the role of PARG, the contribution of free versus protein-bound PAR species, and the extent of AIF translocation. Moreover, there is limited

evidence that clinically relevant PARG inhibitors induce a parthanatos-like response as single agents. Instead, emerging studies have suggested replication-dependent mechanisms (13-16), further complicating the interpretation of PARG inhibitor cytotoxicity.

Beyond these mechanistic uncertainties, it remains unclear whether PARG inhibition can effectively eliminate non-proliferating cancer cells. Therapy-induced senescence (TIS), also referred to as drug-induced senescence, is a durable senescence-like state triggered by anticancer treatments including DNA-damaging agents and CDK4/6 inhibitors (17). Although TIS can impose stable proliferative arrest and thereby contribute to short-term tumor control, senescent-like cancer cells may persist and promote tumor relapse through prolonged survival under cell-cycle arrest (18). Because such cells are relatively refractory to conventional therapies including DNA-damaging agents that preferentially target proliferating cells in S or M phases, alternative strategies capable of eliminating non-proliferating cancer cells are required.

Here, we report the discovery of novel PARG inhibitors and define a previously underappreciated mechanism of PARG inhibitor cytotoxicity. In contrast to earlier models, we find that sensitivity to PARG inhibition is strongly associated with BER deficiency and that cell death is primarily driven by the toxic accumulation of PARylated proteins rather than NAD^+ depletion. Importantly, PARG inhibitor-induced cytotoxicity occurs with minimal evidence of canonical replication stress but is associated with progressive PAR accumulation, early mitochondrial dysfunction, subsequent AIF translocation, and caspase activation. Importantly, this replication-independent mechanism enables effective elimination of cancer cells in G1–arrested states and in TIS. These findings support a model in which excessive PAR accumulation beyond a critical threshold determines cellular fate. Together, these results highlight PARG inhibition as a strategy to eliminate BER-vulnerable and non-proliferating cancer cells that are otherwise relatively refractory to conventional DNA-damaging therapies.

Materials and Methods

Discovery and synthesis of MOD000568 and MOD000582

MOD000568 and MOD000582 were discovered as small molecule PARG inhibitors by Alivexis, Inc. (Tokyo, Japan), and synthesized at Jubilant Biosys Limited (Noida, India), as described in US Patent Application Publication (19).

PARG protein production

Human PARG (residues 448-976) containing the K616A, Q617A, K618A, E688A, K689A, and K690A substitutions (20) was subcloned into a pET28a vector to add an N-terminal TEV protease-cleavable 6×His tag. The plasmid was transformed into *E. coli* BL21-Gold (DE3) cells (Novagen) for recombinant protein expression. Transformed cells were cultured in 2xYT medium supplemented with 50 µg/mL kanamycin at 37°C. When the culture reached an OD_{600} of 0.6, protein expression was induced with 0.5 mM isopropyl-β-D-thiogalactopyranoside (IPTG), followed by incubation at 18°C for approximately 18 h. Harvested cell pellets were lysed by sonication in lysis buffer (50 mM HEPES [pH 7.0], 400 mM NaCl, 5 mM β-mercaptoethanol (β-ME), 10% glycerol, 1% protease inhibitor cocktail, 0.1% Triton X-100, 0.3 mg/mL lysozyme, and 250 U Benzonase nuclease). After centrifugation at 39,000×g for 60 min, the supernatant was filtered through a 0.8-µm membrane (Millipore) and loaded onto 6 mL Ni-Sepharose 6 Fast Flow resin (GE Healthcare). The column was washed with wash buffer (50 mM HEPES [pH 7.0], 400 mM NaCl, 5 mM β-ME, and 10% glycerol). Bound protein was eluted with a 50–500 mM imidazole gradient in the same buffer. The 6×His tag was removed by overnight TEV protease digestion during dialysis against 50 mM HEPES [pH 7.0], 400 mM NaCl, 2 mM DTT, and 10% glycerol at 4°C. The PARG protein was further purified by size-exclusion chromatography on a Superdex 200 column. The purified protein was concentrated to 7 mg/mL for crystallization.

Crystallization and data collection

The PARG protein was incubated with MOD000582 at a 1:2 (protein: compound) molar ratio and concentrated to the final working concentration. Crystallization drops were prepared in

Intelli-Plates by mixing equal volumes of protein solution and reservoir solution. Crystals of the PARG protein in complex with MOD000582 were obtained using the sitting-drop vapor diffusion method in a reservoir solution containing 16% (w/v) PEG 3350, 100 mM PCTP (pH7.2), and 180 mM ammonium sulfate. Crystals suitable for diffraction, typically 40–60 µm in size, appeared within 2–3 days. A 12% glycerol solution prepared in mother liquor was used as a cryoprotectant, and crystals were flash-cooled in liquid nitrogen. Diffraction data for the complex were collected at the Soleil synchrotron facility (PROXIMA-1 beamline). Data were collected to 2.15 Å resolution.

Structure determination and refinement

X-ray diffraction data were processed using XDS. Initial phases were obtained by molecular replacement with MOLREP (CCP4 Suite, v9.0.011), using the previously solved structure of PARG (PDB ID: 4B1H) as the search model. Subsequent model building and inspection of the electron-density maps were performed in COOT (v0.9.8). Ligand fitting into the corresponding electron density was carried out using AFITT (v3.0.1), and the compounds were modeled into their respective binding pockets based on the calculated $F_o - F_c$ and $2F_o - F_c$ maps. Each round of manual model adjustment in COOT was followed by refinement with REFMAC5. The stereochemical quality was assessed using PROCHECK, and the Ramachandran plot indicated good overall geometry. Structural images and superpositions were generated using the software tool PyMOL (v3.1.0, Schrödinger, LLC, RRID:SCR_000305).

Data collection and model statistics are shown in Supplementary Table S1. The atomic coordinates and structure factors have been deposited in the Protein Data Bank under PDB ID 25ND.

PARG enzymatic activity assay

PARG activity assays were performed in streptavidin-coated 96-well plates. The substrate for PARG, a terminally biotinylated poly(ADP-ribose) polymer (R&D systems, #4336-100-02) was diluted to a final concentration of 50 nM in the assay diluent (0.2% BSA in PBS). The diluted substrate solution was added to the assay plate at 200 µL per well, and the plates were then

incubated for 3 h at RT. Following the incubation, unbound substrates were removed by washing the plate with 0.1% PBST four times. The diluted PARG protein (0.5 nM) was pre-incubated with each test compound for 1 h at RT. Then, 100 µL of the resulting mixture was transferred to each well of the poly(ADP-ribose) substrate-coated assay plate, followed by incubation for 18 h at 25°C. After washing the plates, the remaining poly(ADP-ribose) polymers on the plate were detected by using the anti-PAR mouse mAb (Merck, #AM80; 0.5 µg/mL) and the anti-mouse IgG, HRP-linked antibody (Cell Signaling Technology, #7076; 1:2000 dilution). For the detection step, the blank-subtracted OD (450-570) values for each well were plotted, and a four-parameter logistic curve fitting was performed to determine IC_{50} values using GraphPad Prism (GraphPad software).

Cell lines and culture conditions

LoVo (RRID: CVCL_0399) and A549 (RRID: CVCL_0023) cells used for in vivo experiments and MCF7 (RRID: CVCL_0031) cells used for siRNA experiments were obtained from the American Type Culture Collection (ATCC). For other experiments, LoVo cells were obtained from the Japanese Collection of Research Bioresources (JCRB) Cell Bank. MCF-7 WT and XRCC1-KO cells were kindly provided by Dr. Hirota (Tokyo Metropolitan University). TK6 (RRID: CVCL_0561) WT, XRCC1-KO, POLβ-KO, and XRCC1/POLβ -DKO cells were kindly provided by Dr. Sasanuma (Tokyo Metropolitan Institute of Medical Science). HCC1806 (RRID: CVCL_1258), HeLa (RRID: CVCL_0030), and TOV-112D (RRID: CVCL_3612) cells were obtained from ATCC. A549, K562 (RRID: CVCL_0004), and MOLT4 (RRID: CVCL_0013) cells were obtained from the Developmental Therapeutics Program (DTP, NCI). Tree92 (RRID: CVCL_M659) cells were kindly provided by the Department of Hematology, Graduate School of Medicine, Kyoto University.

XRCC1 knockout (KO) (19), POLβ knockout (POLβ-KO) (20), and PARP1 knockout (PARP1-KO) (21) TK6 cells; XRCC1 knockout (XRCC1-KO) MCF7 cells (21); SLFN11 knockout (SLFN11-KO) TOV-112D (22), TREE92 (23), and MOLT4 (24) cells; and SLFN11-overexpressing K562 cells (25) were generated in previous studies. XRCC1/POLβ double knockout (XRCC1/POLβ-DKO) TK6 cells were generated by disrupting POLβ in XRCC1-KO cells using the same strategy as described previously (20).

For in vivo experiments, LoVo and A549 cells were maintained in F-12K medium (Thermo Fisher Scientific, #31800-022) supplemented with 10% fetal bovine serum (FBS; Invitrogen, Thermo Fisher Scientific, #10438-026) and 1% penicillin-streptomycin (Thermo Fisher Scientific, #15140-122).

For siRNA experiments, HeLa cells were cultured in Eagle's Minimum Essential Medium (EMEM; ATCC, #30-2003) supplemented with 10% FBS and 1% penicillin-streptomycin. MCF7 cells were cultured in EMEM (ATCC, #30-2003) supplemented with 10% FBS, 1% penicillin-streptomycin, and 10 μg/mL insulin (Life Technologies, #12585014). HCC1806 cells were cultured in RPMI 1640 medium (ATCC, #A1049101) supplemented with 10% FBS and 1% penicillin-streptomycin.

For other experiments, LoVo, A549, MCF7, and TOV-112D cells were maintained in Dulbecco's modified Eagle medium (DMEM; FUJIFILM Wako Pure Chemical Industries, #044-29765) supplemented with 10% fetal bovine serum (FBS; Gibco, Thermo Fisher Scientific, #A5256701;) and 1% antibiotic-antimycotic solution (100×; Nacalai Tesque, #09366-44). TK6, K562, MOLT4, and TREE92 cells were cultured in RPMI 1640 medium (FUJIFILM Wako Pure Chemical Industries, #189-02145) supplemented with 10% FBS (Gibco, Thermo Fisher Scientific, #A5256701) and 1% antibiotic-antimycotic solution (100×; Nacalai Tesque, # 09366-44). Cells were cultured at 37°C in a humidified incubator with 5% CO_2. All cell lines were routinely tested for mycoplasma contamination and confirmed to be negative.

Drug treatment

Camptothecin (CPT) was obtained from Cayman Chemical (#11694). Talazoparib was obtained from MedChemExpress (#HY-166106). Olaparib was obtained from LC Laboratories (#O-9201). Methyl methanesulfonate (MMS) was obtained from Sigma-Aldrich (#129925-5G). 3-Indoleacetic acid (heteroauxin) was obtained from Nacalai Tesque (#19119-61). Dihydronicotinamide riboside (NRH) was obtained from Biosynth (#MR31174).

Auxin-inducible degron (AID)-mediated protein depletion

BRCA1, BRCA2, and PALB2 were conditionally depleted in TK6 cells using an auxin-inducible degron (AID) system. TK6 cells expressing AID-tagged proteins were treated with 500 μM

auxin (indole-3-acetic acid) for 6 h prior to analysis to induce rapid protein degradation, as previously described (21).

Murine xenograft model

Animal experiments were carried out in accordance with the Institutional Animal Care and Use Committee guidelines of Jubilant Biosys Ltd. (Bengaluru, India). Female BALB/c nude mice were obtained from Vivo BioTech (Hyderabad, India) or the Jackson Laboratory. LoVo and A549 cells were cultured in F12K medium supplemented with 10% FBS and 1% penicillin-streptomycin. Harvested cells were suspended in 1:1 mixture of Matrigel and serum-free medium. The cell suspension ($5–8\times10^6$ cells in 0.2 mL per site) was inoculated subcutaneously into the right flank of each mouse. Once the tumors had reached the desired volume (100–150 mm^3), the mice were selected according to tumor volume and randomly allocated to treatment groups (day 1). MOD568 was dissolved in 0.5% methylcellulose and 0.5% Tween-80 in water, and the suspension was given orally (PO) to individual mice twice daily (BID). Tumor dimensions were measured twice weekly with a caliper, and tumor volume was calculated as 0.5 × length × $width^2$. Body weight was also measured twice weekly, and the relative body weight was calculated by dividing the daily body weight by that of the same mouse on day 1. For immunoblot analysis of LoVo tumor samples, mice were orally administered vehicle or MOD568 PO, BID for 21 days prior to tumor collection.

Antibodies

For in vitro experiments, antibodies against SLFN11 (#sc-515071, RRID: AB_3097730) and total CHK1 (#sc-8408, RRID: AB_627257) were obtained from Santa Cruz Biotechnology; antibodies against BRCA1 (#14823, RRID: AB_2798631), BRCA2 (#10741, RRID: AB_2797730), PAR (#89190, RRID: AB_3716623), XRCC1 (#2735, RRID: AB_2218471), PARP1 (#9532, RRID: AB_659884), cleaved PARP (Asp214) (#5625, RRID: AB_10699459), phospho-CHK1 (Ser345) (#2348, RRID: AB_331212), RPA32/RPA2 (E8X5P) (total RPA2) (#35869, RRID: AB_2799086), histone H3 (#4499, RRID: AB_10544537), and GAPDH (#97166, RRID: AB_2756824) were obtained from Cell Signaling Technology; antibodies against TOM20 (#66777-1-Ig, RRID:

AB_2882123) and AIF (#67791-1-Ig, RRID: AB_2918555) were obtained from Proteintech; α-tubulin (#017-25031, RRID: AB_2943605) was obtained from FUJIFILM Wako Pure Chemical Corporation; phospho-histone H2AX (Ser139) (#05-636, RRID: AB_309864) and PAR (#AM80, RRID:AB_2155072; for PARG activity assays) were obtained from Merck; POLβ (#ab175197) was obtained from Abcam; and phospho-RPA32 (Ser4/Ser8) (#A300-245A, RRID: AB_210547) and PALB2 (#A301-246A, RRID: AB_890607) were obtained from Bethyl Laboratories. For immunoblotting of tumor samples, antibodies against PAR (#4335-MC-100, RRID: AB_2572318) was obtained from Trevigen; PARP1 (#9532, RRID: AB_659884) and GAPDH (#2118, RRID: AB_561053) were obtained from Cell Signaling Technology.

Immunoblotting

Whole-cell lysates were prepared by lysing cells in Laemmli SDS sample buffer followed by boiling. Protein concentrations were determined using an RC DC Protein Assay Kit (Bio-Rad Laboratories, #50000119). Immunoblotting was performed using standard procedures. Primary antibodies were used at a dilution of 1:3000 for PAR, XRCC1, POLβ, PARP1, cleaved PARP1, BRCA1, BRCA2, and PALB2, total CHK1, phospho-CHK1, GAPDH, total RPA2, α-tubulin; 1:5000 for histone H3; and 1:10000 for γH2AX, phospho-RPA2 and 1:15000 for TOM20. Membranes were then incubated with horseradish peroxidase–conjugated secondary antibodies, including anti-rabbit IgG (Promega, #W401B) and anti-mouse IgG (Promega, #W402B). Protein signals were detected using an iBright CL1500 Imaging System (Invitrogen).

For tumor samples, LoVo xenograft tumors were harvested from mice 2 h post-administration of MOD568. Tumor tissues were homogenized in RIPA buffer supplemented with protease and phosphatase inhibitors. Following centrifugation, the supernatant containing the total cell lysate was collected and analyzed by immunoblotting using standard procedures. Primary antibodies were used at a dilution of 1:1,000 for PAR and PARP1, and 1:2,000 for GAPDH. Secondary antibodies used were anti-rabbit IgG HRP-linked antibody (Cell Signaling Technology, #7074S) and anti-mouse IgG HRP-linked antibody (Cell Signaling Technology, #7076S).

Small interfering RNA (siRNA) transfection

TOV-112D cells were transfected with SMARTpool ON-TARGETplus Human XRCC1 siRNA (Horizon Discovery, #L-009394-00-0005) or ON-TARGETplus Non-targeting Control Pool (Horizon Discovery, #D-001810-10-05) as a negative control. siRNAs (10 nM) were transfected using Lipofectamine RNAiMAX Reagent (Invitrogen, #13778-150) according to the manufacturer's instructions. The culture medium was replaced 6 h after transfection, and subsequent experiments were performed 24 h after transfection. Knockdown efficiency was confirmed by immunoblotting.

siRNA loss-of-function screening

HCC1806, MCF7, and HeLa cells were reverse-transfected with SMARTpool ON-TARGETplus siRNAs (Horizon Discovery) targeting genes of interest or a Non-targeting Control (NTC) pool as a negative control. The siRNA was complexed with DharmaFECT1 transfection reagent (Horizon Discovery), and the siRNA-DharmaFECT1 complexes were pre-plated in each well, followed by the addition of cells to achieve a final siRNA concentration of 20 nM. The final volume of DharmaFECT1 per well was 0.01 µL for HCC1806, and 0.02 µL for Hela and MCF7 cells. Forty eight hours post transfection, HCC1806 cells were treated with 3 µM of MOD568, while Hela and MCF7 cells were treated with 30 µM. For vehicle control, cells were also treated with DMSO alone. After 5-day culture, cell viability was quantified using CellTiter-Glo Luminescent Cell Viability Assay (Promega). Each siRNA treatment was performed in duplicate. To evaluate the effect of gene knockdown on compound sensitivity, cell viability was first normalized to the vehicle-treated control within each siRNA condition. To isolate the knockdown-specific effect, these normalized values were then expressed relative to those of the NTC. Lastly, a robust z-score transformation (22) was applied to each cell line independently to enable a direct comparison of knockdown-induced changes in drug sensitivity across multiple cell lines.

Cell viability assays

Cells were seeded in 96-well white plates (SPL Life Sciences, #s30196) at a density of 750–5,000 cells per well in 100 µL of medium. Cells were continuously exposed to the indicated drug concentrations for the indicated time periods in triplicate. Cell viability was measured using an ATPlite 1step Luminescence ATP Detection Assay System (Revvity, #6016731) or RealTime-Glo™ MT Cell Viability Assay (Promega, #G9713) according to the manufacturer's instructions. Luminescence was measured using a Synergy LX Multi-Mode Reader (BioTek). Cell viability (%) was normalized to untreated controls.

Immunofluorescence analysis

TK6 cells were cytospun onto SuperFrost Plus microscope slides (Thermo Fisher Scientific, #J1820AMNZ) using a Cytospin 4 Cytocentrifuge (Thermo Fisher Scientific), whereas MCF7 cells were grown on chamber slides (Watson, #192-004). Cells were fixed either with 4% paraformaldehyde in PBS for 10 min (TK6) or with 100% methanol at -30 °C for 15 min (MCF-7). For TK6 cells, permeabilization was performed with 0.1% Triton X-100 in PBS for 5 min. Cells were blocked with 4% bovine serum albumin (BSA) in PBST for 30 min (TK6) or 3% BSA in PBS for 10 min (MCF7), followed by overnight incubation at 4 °C with primary antibodies against PAR (1:300) for TK6, or PAR (1:300), TOM20 (1:500), and AIF (1:500) for MCF7 diluted in blocking buffer. After washing, cells were incubated with appropriate secondary antibodies, including goat anti-rabbit IgG (H+L) cross-adsorbed Alexa Fluor 488 (Invitrogen, #A-11008, RRID: AB_143165) and goat anti-mouse IgG (H+L) cross-adsorbed Alexa Fluor 568 (Invitrogen, #A-11004, RRID: AB_2534072), at a dilution of 1:1000 in 3–5% BSA/PBST for 1–4 h at room temperature. After washing, cells were mounted with Fluoroshield Mounting Medium with DAPI (Abcam, #AB104139). Images were acquired using a LSM 900 confocal microscope (ZEISS) or a BZ-X1000 fluorescence microscope (KEYENCE).

Measurement of NAD(H) levels

NAD(H) levels were measured using a luminescence-based assay kit (NAD/NADH-Glo Assay, Promega, #G9072) according to the manufacturer's instructions. Cells were treated with

MOD582 in the presence or absence of NRH for the indicated times. Luminescence was measured using a Synergy LX Multi-Mode Reader (BioTek).

Cell cycle analysis by flow cytometry

Cells were incubated with 10 μM EdU for 1 h using a Click-iT Plus EdU Alexa Fluor 488 Flow Cytometry Assay Kit (Invitrogen, #C10633) according to the manufacturer's instructions. DNA content was assessed by propidium iodide (PI) staining (Nacalai Tesque, #25535-16). Data were acquired using a CytoFLEX flow cytometer (Beckman Coulter) and analyzed with FlowJo software (BD Biosciences).

Subcellular fractionation

Cytosolic and mitochondrial fractions were isolated using a Mitochondria Isolation Kit for Cultured Cells (Thermo Fisher Scientific, #89874) following the reagent-based protocol according to the manufacturer's instructions. Fraction purity was confirmed by immunoblotting for α-tubulin (cytosolic marker) and TOM20 (mitochondrial marker). PAR levels were analyzed in each fraction by immunoblotting.

Metabolic flux analysis

Metabolic flux was analyzed using a Seahorse XFp Extracellular Flux Analyzer (Agilent Technologies). Cells were seeded in Seahorse XFp Cell Culture Miniplates (Agilent Technologies, #103025-100) at a density of 1×10^4 cells per well and incubated for 24 h prior to the assay. Cells were treated with MOD582 (10 μM) for a total of 6 h prior to analysis, including a 1 h incubation period in a CO_2-free incubator. Cells were incubated in XF DMEM Medium (Agilent Technologies, #03575-100) supplemented with 10 mM glucose, 1 mM pyruvate, and 2 mM glutamine, and equilibrated at 37 °C in a CO_2-free incubator for 1 h. MOD582 was maintained in the assay medium throughout the equilibration period. Oxygen consumption rate (OCR) and extracellular acidification rate (ECAR) were measured using the Seahorse XFp Cell Mito Stress Test Kit (Agilent Technologies, #103010-100), and ATP

production rates were determined using the Seahorse XFp Real-Time ATP Rate Assay Kit (#103591-100, Agilent Technologies), according to the manufacturer's instructions. For the Mito Stress Test, after three baseline measurements, 1 μM oligomycin, 1 μM carbonyl cyanide 4-(trifluoromethoxy)phenylhydrazone (FCCP), and 0.5 μM antimycin A/rotenone were sequentially injected. For the ATP rate assay, 1.5 μM oligomycin and 0.5 μM antimycin A/rotenone were sequentially injected.

Induction of G1 arrest by palbociclib

Cells were treated with palbociclib (1000 nM) (Selleck Chemicals, #S1579) for 24 h to induce G1 cell-cycle arrest. Cells were either harvested for cell-cycle analysis or subsequently used for drug treatment experiments. For DNA content analysis, cells were fixed and stained with propidium iodide (PI) (Sigma-Aldrich, #P4170). Data were acquired using a CytoFLEX flow cytometer (Beckman Coulter) and analyzed with FlowJo software (BD Life Sciences). Cell-cycle distribution was determined based on DNA content histograms.

Induction of therapy-induced senescence (TIS) and SA-β-galactosidase staining

Cells were seeded in 6-well plates (IWAKI, #3810-006N) and treated with palbociclib (1000 nM) for 72 h to induce senescence-like phenotypes. Cells were stained for senescence-associated β-galactosidase (SA-β-gal) activity using a Senescence β-Galactosidase Staining Kit (Cell Signaling Technology, #9860) according to the manufacturer's instructions. After addition of the staining solution, cells were incubated for 48 h in a CO_2-free incubator. Senescence-like cells were identified based on SA-β-gal positivity as well as characteristic morphological changes, including enlarged and flattened cell morphology. Bright-field images were acquired using an EVOS M3000 Imaging System (Thermo Fisher Scientific).

Clonogenic survival assay

Clonogenic assays were performed in MCF7 XRCC1-KO cells. Cells were seeded in 96-well clear plates (IWAKI, #3860-096) and allowed to attach overnight. Cells were either untreated or

pretreated with palbociclib (1000 nM) for 72 h, followed by treatment with CPT or MOD582 in the presence or absence of MMS (0.0001%). After 72 h, cells were fixed and stained with 0.2% crystal violet solution (Sigma-Aldrich, #V5265). Stained cells were washed, air-dried, and subsequently solubilized with 33% acetic acid (FUJIFILM Wako Pure Chemical Industries, #017-00251). Absorbance was measured using a Varioskan LUX multimode microplate reader (Thermo Fisher Scientific) to quantify cell viability. Cell viability was normalized to untreated controls.

Statistical analysis

Data are presented as mean ± standard deviation (SD). Details of technical and biological replicates are described in each figure legend. Tumor volume and body weight data are presented as mean ± standard error of the mean (SEM). Statistical analyses were performed using GraphPad Prism (GraphPad Software, version 10.6.1). Two-group comparisons were performed using an unpaired Welch's t-test. Multiple comparisons were analyzed using one-way ANOVA followed by Tukey's test, or by Dunnett's test for tumor-volume comparisons. *P* values < 0.05 were considered statistically significant. Significance is indicated as follows: ns, not significant; **P* < 0.05; ***P* < 0.01; ****P* < 0.001; *****P* < 0.0001**.**

Data availability

The structural data have been deposited in the Protein Data Bank (PDB ID: 25ND). Unprocessed data will be made publicly available in Mendeley Data upon publication. All other data are included in this article and its supplementary information files or are available from the corresponding author upon reasonable request.

Results

Novel PARG inhibitors induce PAR accumulation and anticancer effects *in vitro* and *in vivo*

To establish a pharmacologic framework for interrogating the mechanism of PARG inhibition, we identified two novel PARG inhibitors, MOD000568 (MOD568) and MOD000582 (MOD582) (Fig. 1A), through an integrated *in silico* screening and medicinal chemistry approach. The biochemical activity of these compounds was evaluated using a PAR ELISA-based assay. While MOD568 showed moderate inhibitory activity (IC_{50} = 0.018 μM), MOD582 exhibited low single-digit nanomolar inhibitory activity (IC_{50} = 0.0017 μM) (Fig. 1B). Accordingly, MOD582 represents approximately a 10-fold increase in biochemical potency compared with the previously reported PARG inhibitor PDD00017273 (23).

To characterize the binding mode of MOD582, we determined the co-crystal structure of the human PARG catalytic domain in complex with the inhibitor (Table S1). The structure, resolved at 2.15 Å resolution, revealed that MOD582 directly occupies the PAR-binding pocket and forms a sulfonamide-mediated hydrogen-bond network with Ile726, Glu727, Gln754, and Tyr792 (Fig. 1C). Notably, the dihydroisobenzofuran side chain of MOD582 forms an additional hydrogen bond with Gly724, an interaction not observed in the previously reported inhibitor PDD00017299 (24), which likely contributes to the enhanced inhibitory potency of MOD582.

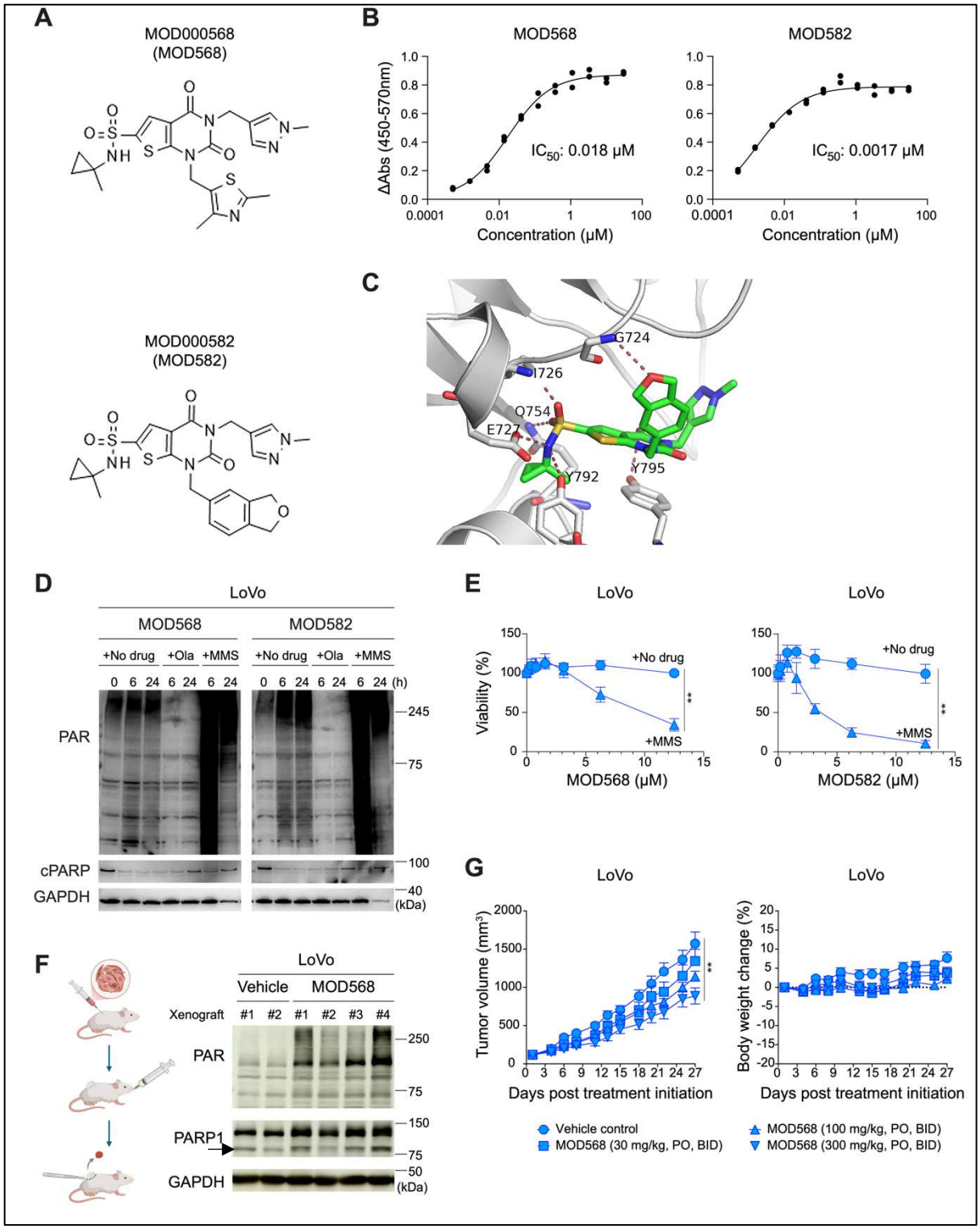


Figure 1. Biochemical and functional characterization of the PARG inhibitors MOD568 and MOD582 *in vitro* and *in vivo*.

A Chemical structures of MOD568 and MOD582. **B** PARG inhibitory activity of the compounds in the PAR ELISA assay. Data represent absorbance measurements (n = 2, technical replicates). **C** X-ray structure of MOD582 (green) bound in the binding pocket of the human PARG catalytic domain, with hydrogen bonds (red dotted lines). **D** Immunoblots of PARylated proteins. Cells were treated with MOD568 (10 μM) or MOD582 (10 μM), with or without the PARP inhibitor olaparib (10 μM) or the alkylating agent MMS (0.00025%) for the indicated durations. PAR levels in whole-cell lysates were examined by immunoblotting. GAPDH served as a loading

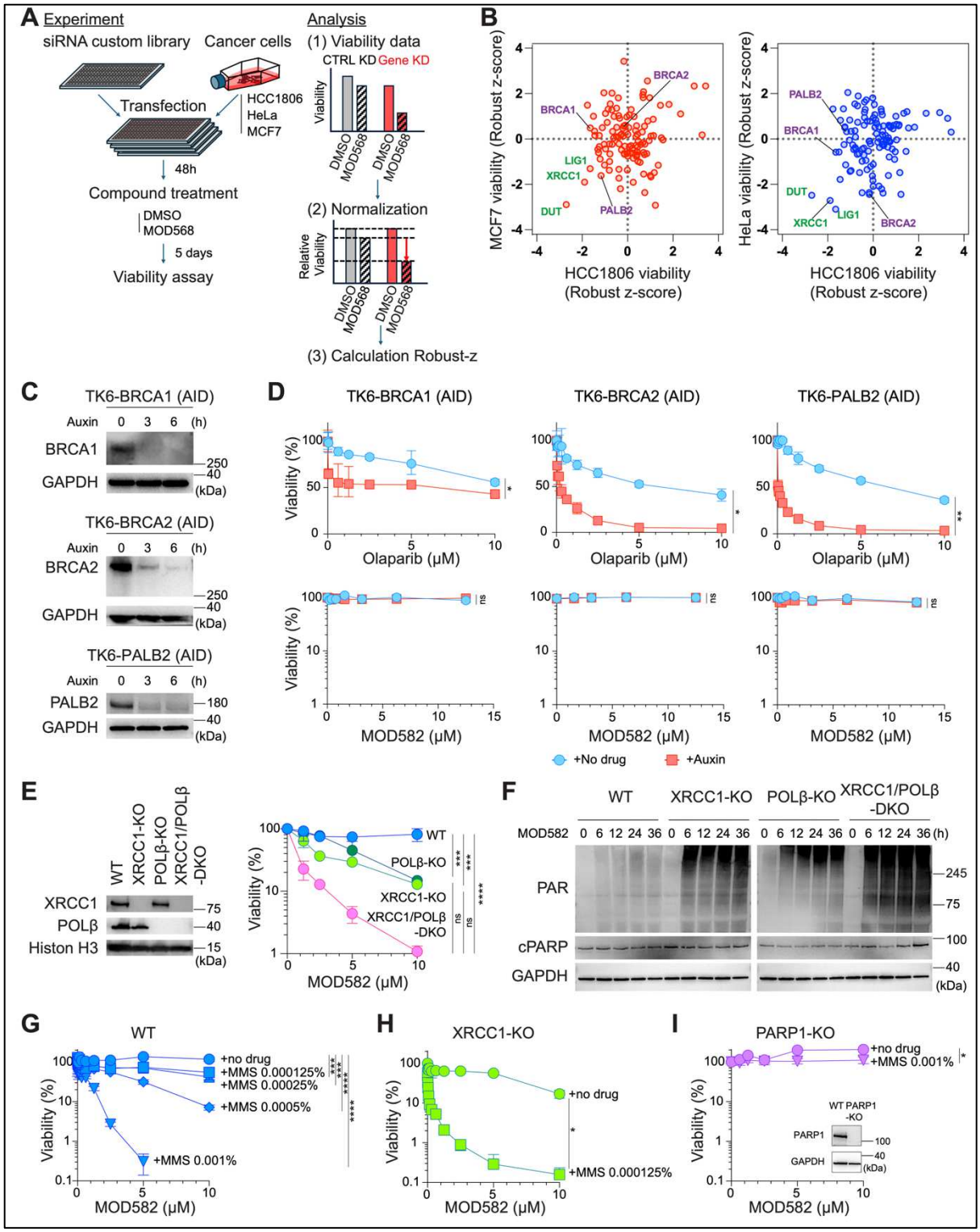
control. **E** Viability of LoVo cells treated with MOD568 or MOD582 with or without MMS (0.000125%). Cell viability was assessed 72 h after treatment and normalized to untreated controls. Data represent mean ± SD (n=3, technical replicates) and represent one of two biologically independent experiments. $^{**}P < 0.01$. **F** Schematic overview of the tumor cell inoculation procedure (left) and immunoblot analysis of PAR, PARP1, and GAPDH in LoVo tumor lysates (right). The arrow indicates cleaved PARP1. **G** Antitumor activity (left) and body weight change (right) in the LoVo xenograft model. Data represent mean ± SEM (n = 8). $^{**}P < 0.01$ versus vehicle control. PO, orally; BID, twice daily.

To examine the pharmacological potency of MOD568 and MOD582, we used LoVo (colorectal cancer) and A549 (lung cancer), since both cell lines have been used in early studies of PARG biology (25, 26). Treatment with either MOD568 or MOD582 led to a time-dependent accumulation of PARylated proteins (Fig. 1D and S1A). Co-treatment with the PARP inhibitor olaparib suppressed this accumulation, indicating that this PARylation depends on PARP activity (Fig. 1D and S1A). In contrast, treatment with the alkylating agent methyl methanesulfonate (MMS) markedly enhanced PARylation in the presence of PARG inhibitors, consistent with increased PAR synthesis in response to DNA damage (Fig. 1D and S1A). Although MOD568 or MOD582 alone caused minimal cytotoxicity in LoVo and A549 cells, co-treatment with MMS induced cleaved PARP1, a hallmark of apoptosis, and significant reduction of cell viability in a dose-dependent manner (Fig. 1D–E and S1A–B), suggesting that excessive PARylation contributes to cytotoxicity.

We then established a LoVo subcutaneous xenograft model in mice. Tumors from MOD568-treated mice showed marked accumulation of PARylated proteins compared with vehicle-treated controls (Fig. 1F), confirming target engagement of PARG inhibition *in vivo*. Cleaved PARP1 was also detected in a subset of MOD568-treated tumors, consistent with induction of apoptosis. MOD568 significantly suppressed tumor growth in both LoVo and A549 xenograft models when administered as monotherapy, with minimal body weight loss (Fig. 1G and S1C). These results demonstrate that MOD568 is well tolerated at doses up to 300 mg/kg twice daily in mice and exhibits single-agent antitumor activity associated with increased PARylation in tumor cells. Together, these results establish MOD568 and MOD582 as pharmacologically active PARG inhibitors that induce sustained PAR accumulation and provide a tractable system for mechanistic studies *in vitro* and *in vivo*.

BER deficiency, more consistently than HR deficiency, sensitizes cancer cells to PARG inhibition

To identify genetic contexts that enhance susceptibility to PARG inhibition, we performed a focused loss-of-function siRNA screen targeting DNA repair and nucleotide metabolism pathways (Table S2). The screen was conducted in three cancer cell lines (MCF-7, HCC1806, and HeLa), and compound effects were normalized to non-targeting controls (Fig. 2A). Robust z-score analysis identified common hits across all three cell lines, including XRCC1 (a central scaffold protein coordinating BER), LIG1 (a DNA ligase responsible for sealing repair-associated DNA nicks) and DUT (a dUTPase that prevents uracil misincorporation into DNA) (27) (Fig. 2B). Notably, depletion of these genes is expected to increase endogenous DNA lesions that require BER, thereby promoting PARP activation. Depletion of HR genes such as BRCA1, BRCA2, and PALB2 also enhanced sensitivity to PARG inhibition, but this effect was not consistent across the three cell lines (Fig. 2B).



508

509 **Figure 2. Deficiency of BER-related genes or proteins confers the sensitivity to the PARG inhibitors.**
510 **A** Schematic overview of the workflow for the loss-of-function siRNA screen. **B** Effect of MOD568 on cell
511 viability in the siRNA screen. Minus numbers indicate hypersensitivity by the gene knockdown compared to
512 control knockdown. Representative siRNAs targeting BER- and HRD-related genes are shown in green and
513 purple, respectively. **C** TK6 cells expressing auxin-inducible degron (AID)-tagged BRCA1, BRCA2, or PALB2 were
514 treated with auxin (500 μM) for the indicated times. Protein degradation was confirmed by immunoblotting. **D**
515 TK6 cells with auxin-inducible degradation of BRCA1, BRCA2, or PALB2 protein were treated with olaparib or

MOD582 with or without auxin (500 μM). Cell viability was assessed 72 h after MOD582 treatment and normalized to untreated controls. Data represent mean ± SD (n=3, technical replicates) and represent one of three biologically independent experiments. *P < 0.05, **P < 0.01. ns, not significant. **E** Left: Confirmation of gene knockout in the indicated cell lines. Right: Cell viability of WT and KO cells after MOD582 treatment. Cell viability was assessed 72 h after MOD582 treatment and normalized to untreated controls. Data represent mean ± SD (n=3, technical replicates) and represent one of two biologically independent experiments. ***P < 0.001, ****P < 0.0001. **F** Immunoblotting using anti-PAR antibody. MOD582 (10 μM) was applied for the indicated times. Data represent one of three biologically independent experiments. **G-I** Viability of TK6 WT, XRCC1-KO, and PARP1-KO cells treated with the different doses of MOD582 with or without MMS. Cell viability was assessed 72h after treatment and normalized to untreated controls. The absence of PARP1 in PARP1-KO cells was confirmed by immunoblotting. Data represent mean ± SD (n=3, technical replicates) and represent one of two biologically independent experiments. *P < 0.05, ***P < 0.001, ****P < 0.0001.

To validate this observation, we used the human B lymphoblastoid cell line TK6, in which BRCA1, BRCA2, or PALB2 can be conditionally degraded using an auxin-inducible degron system (28) (Fig. 2C). Although depletion of these HR factors markedly increased sensitivity to the PARP inhibitor olaparib, these cells remained largely insensitive to MOD582 (Fig. 2D), indicating that HR deficiency alone is not sufficient to confer sensitivity to PARG inhibition in TK6 cells. We therefore focused on BER for further investigation. TK6 cells lacking XRCC1, POLB (a DNA polymerase that fills short gaps during BER), or both genes exhibited markedly increased sensitivity to MOD582 compared with wild-type (WT) cells, with the double knockout showing the strongest effect (Fig. 2E, S2A). Consistent with this enhanced sensitivity, MOD582 treatment induced greater accumulation of PARylated proteins and cleaved PARP1 in the BER-deficient cells relative to WT cells (Fig. 2F).

Despite the minimal toxicity of MOD582 in WT TK6 cells, the addition of MMS sensitized WT cells in an MMS dose-dependent manner, with hyperaccumulation of PARylation (Fig. 2G and S2B). The effect of MMS was much stronger in XRCC1-deficient cells than WT cells (Fig. 2H). In contrast, PARP1-knockout TK6 cells were resistant to the MOD582–MMS combination, indicating that PARP1-dependent PARylation is required for the observed cell death (Fig. 2I). These findings identify BER deficiency as the most consistent sensitizing context for PARG inhibition and indicate that increased PARP-dependent PAR accumulation underlies this hypersensitivity.

Toxic PAR accumulation, rather than NAD+ depletion, primarily drives PARG inhibitor cytotoxicity

Because both PAR accumulation and NAD^+ consumption can accompany sustained PARP activity, we next asked which of these processes is most directly linked to cell death after PARG inhibition. NRH (dihydronicotinamide riboside), a precursor of NAD^+ that restores NAD^+ without inhibiting PARP activity (27), increased total intracellular NAD^+/NADH in our system (Fig. 3A) and, further enhanced PAR accumulation (Fig. 3B). Importantly, under these conditions, cell death was further enhanced rather than suppressed (Fig. 3C-D). Together, these results indicate that toxic PAR overload, rather than intracellular NAD^+ depletion, primarily drives cell death following PARG inhibition.

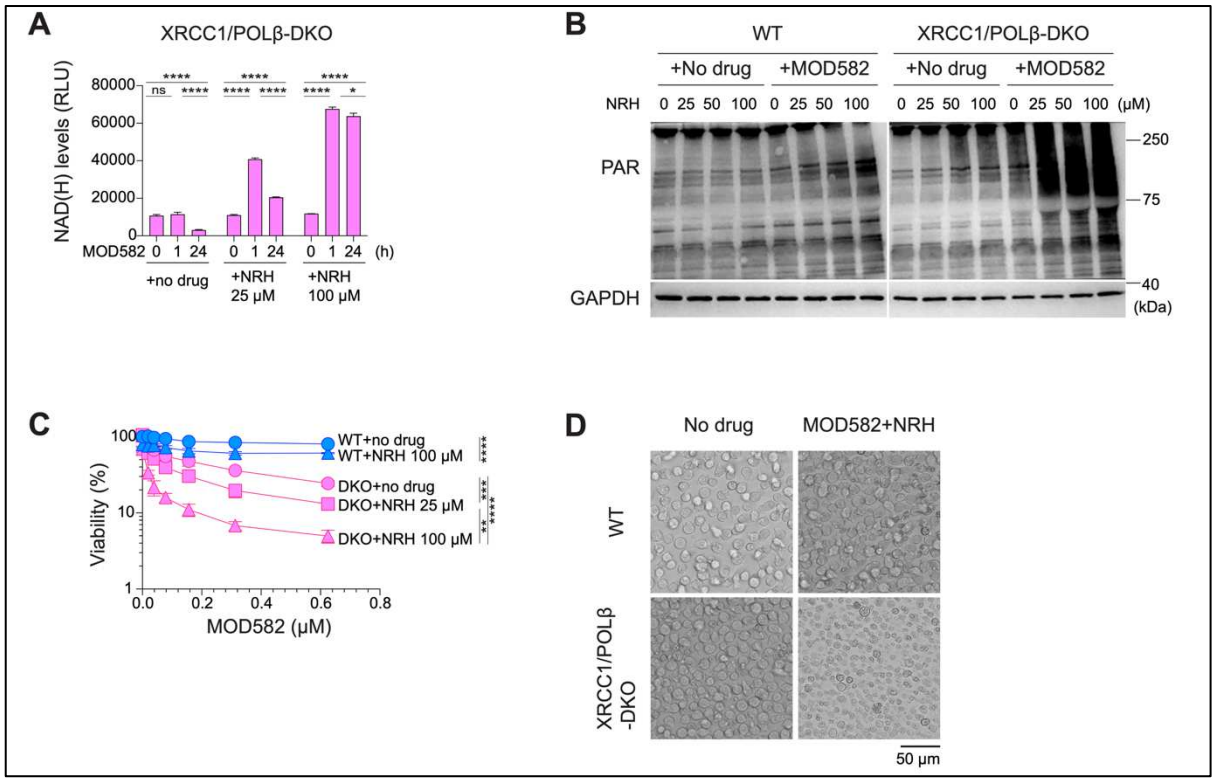


Figure 3. Toxic PAR accumulation rather than NAD+ depletion drives PARG inhibitor cytotoxicity.
A NAD^+/NADH levels in TK6 XRCC1/POLβ-DKO cells treated with MOD582 (10 μM) with or without NRH (25 or 100 μM). Data represent mean ± SD (n=3, technical replicates) and represent one of two biologically independent experiments. *P < 0.05, ****P < 0.0001. ns, not significant. **B** Accumulation of PARylated proteins induced by the combination of MOD582 and NRH. TK6 WT and XRCC1/POLβ-DKO cells were treated with MOD582 (1 μM) with or without NRH (0–100 μM) for 6 h. Data represent one of three biologically independent experiments. **C** Viability of TK6 WT and XRCC1/POLB-DKO cells treated with MOD582 with or without NRH (25 or 100 μM). Cell viability was assessed 72 h after treatment and normalized to untreated controls. Data represent mean ± SD (n=3, technical replicates) and represent one of three biologically independent experiments. **P < 0.01, ***P < 0.001, ****P < 0.0001. **D** Representative bright-field images of TK6 WT and XRCC1/POLβ-DKO cells following treatment with MOD582 (1 μM) with or without NRH (100 μM) for 48 h. Scale bar, 50 μm.

PARG inhibition induces cell death largely independently of canonical replication stress pathways

Given the emerging view that PARG inhibitors act primarily through replication-associated stress, we next examined whether MOD582 induces canonical features of replication stress in sensitive BER-deficient models. To address this, we used breast cancer MCF7 and ovarian cancer TOV112D cells because TK6 cells lack thymidine kinase activity and are therefore unable to incorporate BrdU or EdU for cell cycle analysis (29). XRCC1-deficient models were established in both cell lines using gene knockout or siRNA-mediated knockdown (Fig. 4A). Consistent with our observations in TK6 cells, MOD582 treatment induced accumulation of PARylated proteins, which was further enhanced in XRCC1-deficient cells (Fig. 4B). XRCC1-deficient MCF7 and TOV112D cells also exhibited markedly increased sensitivity to MOD582 compared with their respective control cells (Fig. 4C).

EdU incorporation–based cell cycle analysis showed that the topoisomerase I inhibitor camptothecin (CPT) (30) reduced the fraction of EdU-positive S-phase cells and increased the G2 population, consistent with its replication-dependent DNA-damaging activity (Fig. 4D). In contrast, MOD582 treatment reduced the S-phase population by approximately half in XRCC1-deficient MCF7 cells; however, a substantial fraction of cells remained EdU-positive, indicating ongoing DNA synthesis. Moreover, MOD582 did not substantially alter EdU incorporation or cell cycle distribution in XRCC1-deficient TOV112D cells (Fig. 4D). Consistent with these observations, CPT strongly induced canonical replication stress markers, including γH2AX, CHK1 phosphorylation, and RPA2 phosphorylation, whereas MOD582 caused only minimal activation of these pathways (Fig. 4E). Nevertheless, cleaved PARP1, a hallmark of apoptosis, was detected following MOD582 treatment at 24 h and 48 h in XRCC1-deficient MCF7 and TOV112D cells, respectively (Fig. 4E). Consistently, CHK1 phosphorylation was not observed in TK6 BER mutant cells under hypersensitive conditions (Fig. S3A), further supporting that MOD582 does not induce robust replication stress signaling.

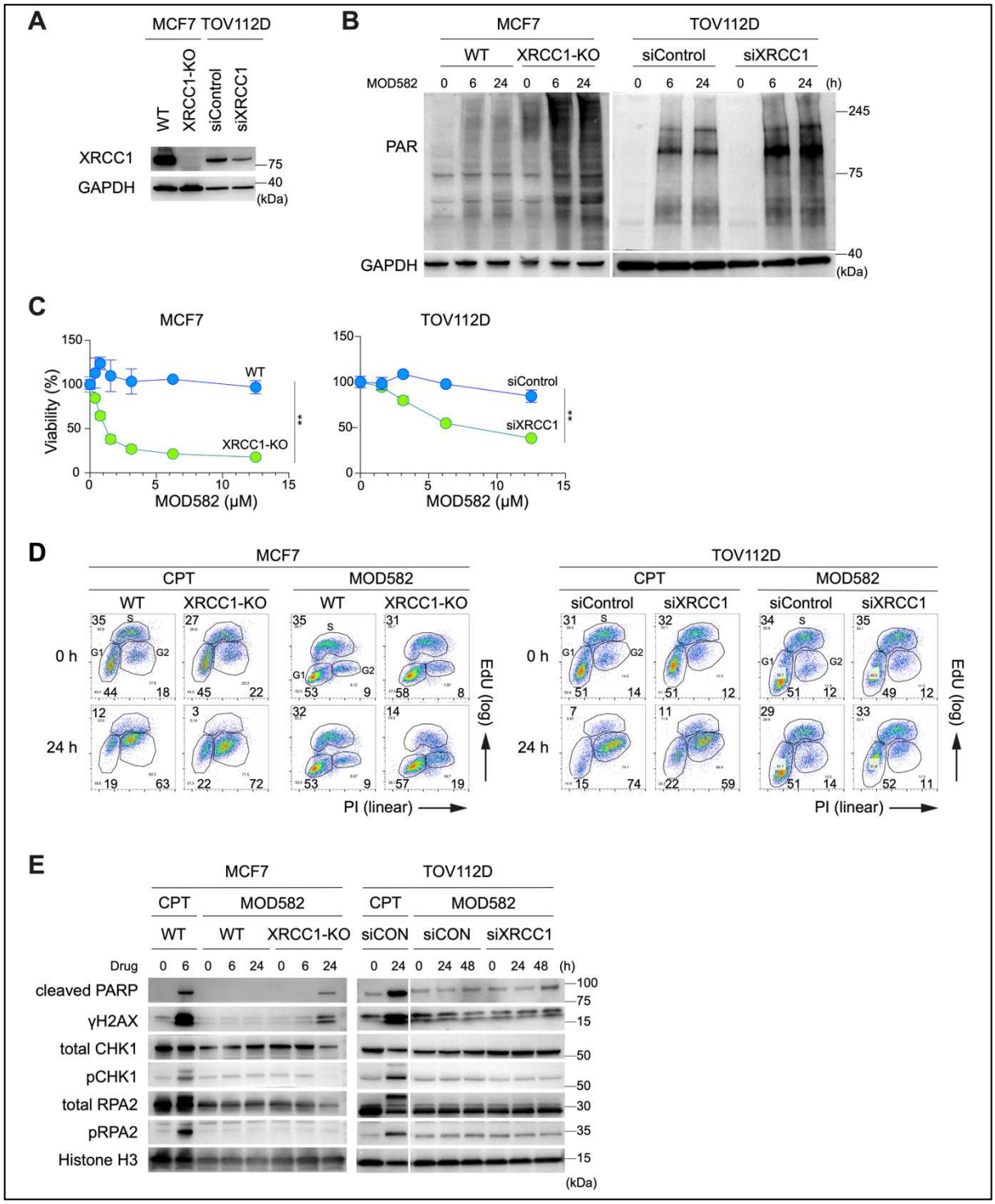


Figure 4. PARG inhibition induces cell death independently of canonical replication stress.
A XRCC1 protein expression in the indicated cell lines. Data represent one of two biologically independent experiments. **B** Accumulation of PARylated proteins. Cells were treated with MOD582 (10 μM) for the indicated times. **C** Viability of the indicated cell lines treated with MOD582. Data were obtained 72 h after MOD582 treatment and normalized to untreated controls. Data represent mean ± SD (n=3, technical replicates) and represent one of two biologically independent experiments. $^{**}P < 0.01$. **D** Cell-cycle distribution following treatment with camptothecin (CPT, 25 nM) or MOD582 (10 μM) for 24h. Cells were analyzed by EdU incorporation and propidium iodide (PI) staining, followed by flow cytometry. Data represent one of two biologically independent experiments. The population (%) corresponding to G1-, replicating S-, G2-phase were

shown in each panel. **E** The indicated cells were treated with CPT (10 μM) or MOD582 (10 μM) for the indicated times, and cleaved PARP, γH2AX, total and phospho-CHK1 (pCHK1), total and phospho-RPA2 (pRPA2) were examined. Histone H3 served as a loading control. Data represent one of three biologically independent experiments.

As an additional approach, we assessed the effect of SLFN11 on cytotoxicity (31, 32). SLFN11 is a replication stress sensitizer that promotes cell death by blocking replication through binding to single-stranded DNA (ssDNA), and by blocking translation (32-34). Furthermore, SLFN11 sensitizes cancer cells to PARP inhibitors by inducing ssDNA gaps behind replication forks (35). Consistent with the lack of replication stress, MOD582-induced cytotoxicity was not affected by SLFN11 status in four paired SLFN11-proficient and SLFN11-knockout cell models, whereas CPT sensitivity was significantly greater in the presence of SLFN11 (Fig. S3B-C). Together, these findings suggest that PARG inhibitor–induced cell death arises through a mechanism distinct from replication-dependent or ssDNA gap dependent cytotoxic pathways.

PARG inhibition induces mitochondrial dysfunction and parthanatos-like signaling

We next asked what downstream events might account for replication-independent, PAR-driven cell death induced by PARG inhibition. Immunofluorescence analysis revealed a time-dependent accumulation of PAR signals in the cytoplasm and in association with mitochondria compartment following MOD582 treatment in MCF7 XRCC1-KO cells (Fig. 5A, B). Nuclear translocation of apoptosis-inducing factor (AIF) became evident at later time points, with minimal changes at 6 hours but robust nuclear accumulation observed at 24 and 36 hours (Fig. 5C).

Notably, mitochondrial dysfunction preceded AIF translocation, as evidenced by an early reduction in mitochondrial ATP production and oxygen consumption rate (OCR), a measure of oxidative phosphorylation, as early as 6 hours after MOD582 treatment, without a compensatory increase in extracellular acidification rate (ECAR), an indicator of glycolytic activity (Fig. 5D–F). Collectively, these findings suggest that sustained PAR accumulation engages a parthanatos-like cell death program characterized by early mitochondrial dysfunction followed by AIF nuclear translocation. These responses were observed predominantly in BER-deficient cells, consistent with the concept that excessive PAR

accumulation beyond a critical threshold initiates a replication-independent cell death program.

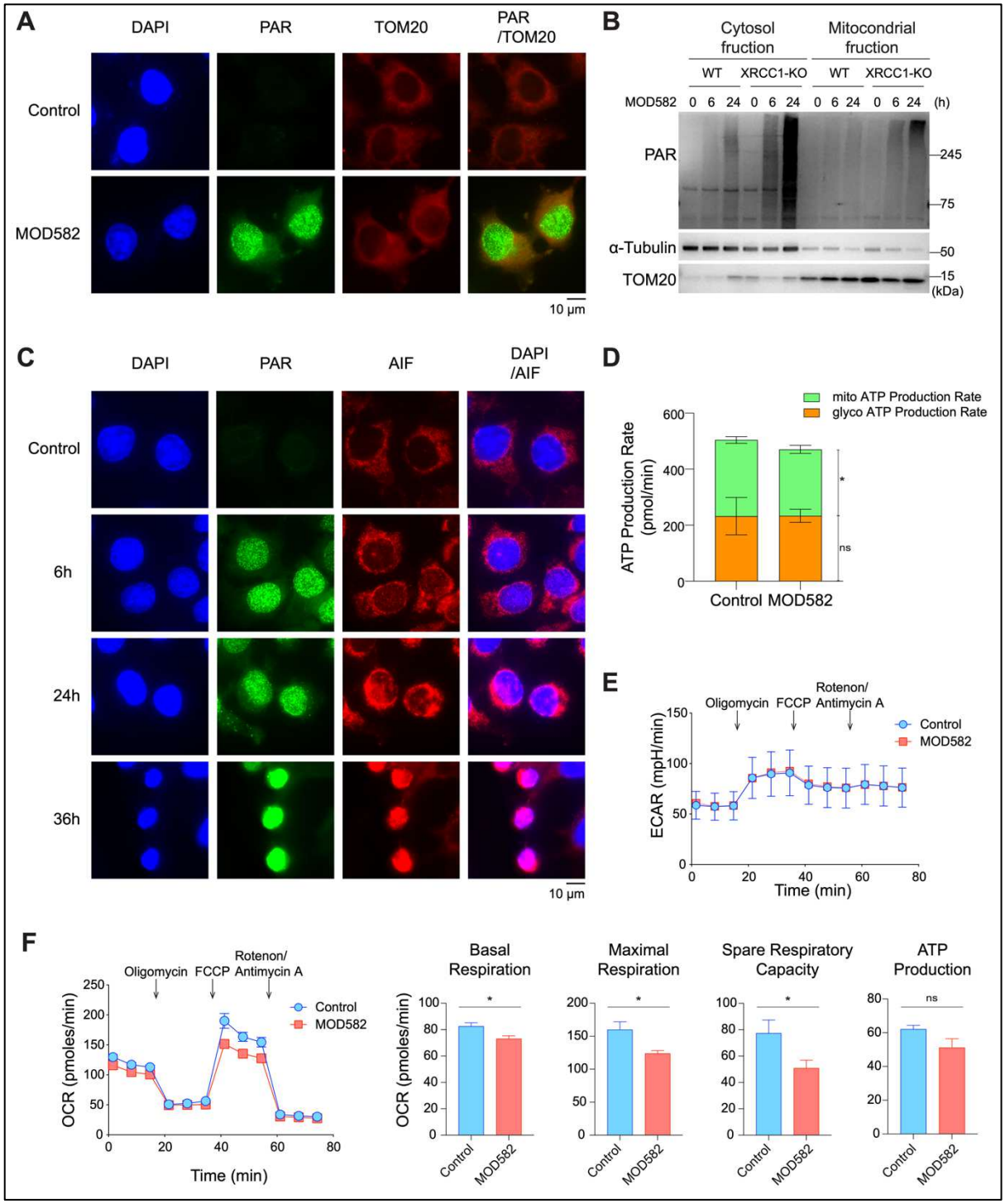


Figure 5. PAR accumulation triggers nuclear translocation of AIF and mitochondrial dysfunction.

A Immunofluorescence analysis of MCF7 XRCC1-KO cells treated with MOD582 (10 μM) for 6 h. Cells were stained for PAR and the mitochondrial marker TOM20, and nuclei were counterstained with DAPI. Representative images are shown. Scale bar, 10 μm. **B** Immunoblotting using cytosolic and mitochondrial fractions. Each fraction was isolated from MCF7 WT and XRCC1-KO cells treated with MOD582 (10 μM). α-Tubulin and TOM20 served as cytosolic and mitochondrial markers, respectively. Data represent one of three biologically independent

experiments. **C** Immunofluorescence analysis of MCF7 XRCC1-KO cells treated with MOD582 (10 µM) for the indicated times. Cells were stained for PAR and AIF, and nuclei were counterstained with DAPI. Representative images are shown. Scale bar, 10 µm. **D-F** Mitochondrial function analyzed using Seahorse extracellular flux assays. MCF7 XRCC1-KO cells were treated with MOD582 (10 µM) for 6 h. **D** Real-time ATP production rate showing mitochondrial ATP production (mito ATP) and glycolytic ATP production (glyco ATP). Data represent mean ± SD (n=3, technical replicates) and represent one of two biologically independent experiments. *P < 0.05. ns, not significant. **E, F** Mitochondrial stress test showing extracellular acidification rate (ECAR; E) and oxygen consumption rate (OCR; F) over time. Oligomycin, FCCP, and rotenone/antimycin A were sequentially injected at the indicated time points. (F, right) Mitochondrial respiration parameters, including basal respiration, maximal respiration, spare respiratory capacity, and ATP production, were quantified. Data represent mean ± SD (n=3, technical replicates) and represent one of three biologically independent experiments. *P < 0.05. ns, not significant.

This replication-independent mechanism enables elimination of G1-arrested and senescence-like cancer cells

A key implication of replication-independent, PAR-driven cell death is that PARG inhibition may eliminate non-proliferating cancer cells that evade conventional therapies. We therefore asked whether MOD582 retains cytotoxic activity under G1 arrest and in therapy-induced senescence-like states, two settings that often escape conventional replication-dependent chemotherapies. Flow cytometry confirmed efficient G1 arrest following treatment with a clinically approved CDK4/6 inhibitor palbociclib in both MCF7 wild-type and XRCC1-deficient cells (Fig. 6A). As expected, the replication-dependent drug CPT exhibited markedly reduced cytotoxicity under G1-arrest conditions (Fig. 6B left). Similarly, sensitivity to the PARP inhibitor talazoparib was attenuated in G1-arrested cells (Fig. 6B middle). In contrast, MOD582 retained strong cytotoxic activity in XRCC1-deficient cells even under G1-arrest conditions (Fig. 6B right). Comparable results were obtained in TK6 wild-type and XRCC1-knockout cells (Fig. S4A-B).

To model therapy-induced senescence (TIS), MCF7 XRCC1-deficient cells were treated with palbociclib for three days, resulting in a senescence-like phenotype characterized by enlarged cell morphology and increased β-galactosidase activity (Fig. 6C). MOD582 treatment induced robust accumulation of PARylated proteins in XRCC1-deficient cells regardless of the proliferative state (Fig. 6D). Clonogenic assays revealed that MOD582, in combination with a low, minimally cytotoxic dose of MMS (Fig. S4B), efficiently eliminated senescence-like cells, resulting in near-complete loss of colony formation (Fig. 6E right). In contrast, CPT failed to eradicate the senescence-like cell population (Fig. 6E left). Together, these results

demonstrate that PARG inhibition can retain cytotoxicity in non-proliferating and senescence-like cancer cells, revealing a mechanistically distinct and therapeutically relevant vulnerability that may be exploited to target cell populations that are otherwise refractory to conventional DNA-targeting agents.

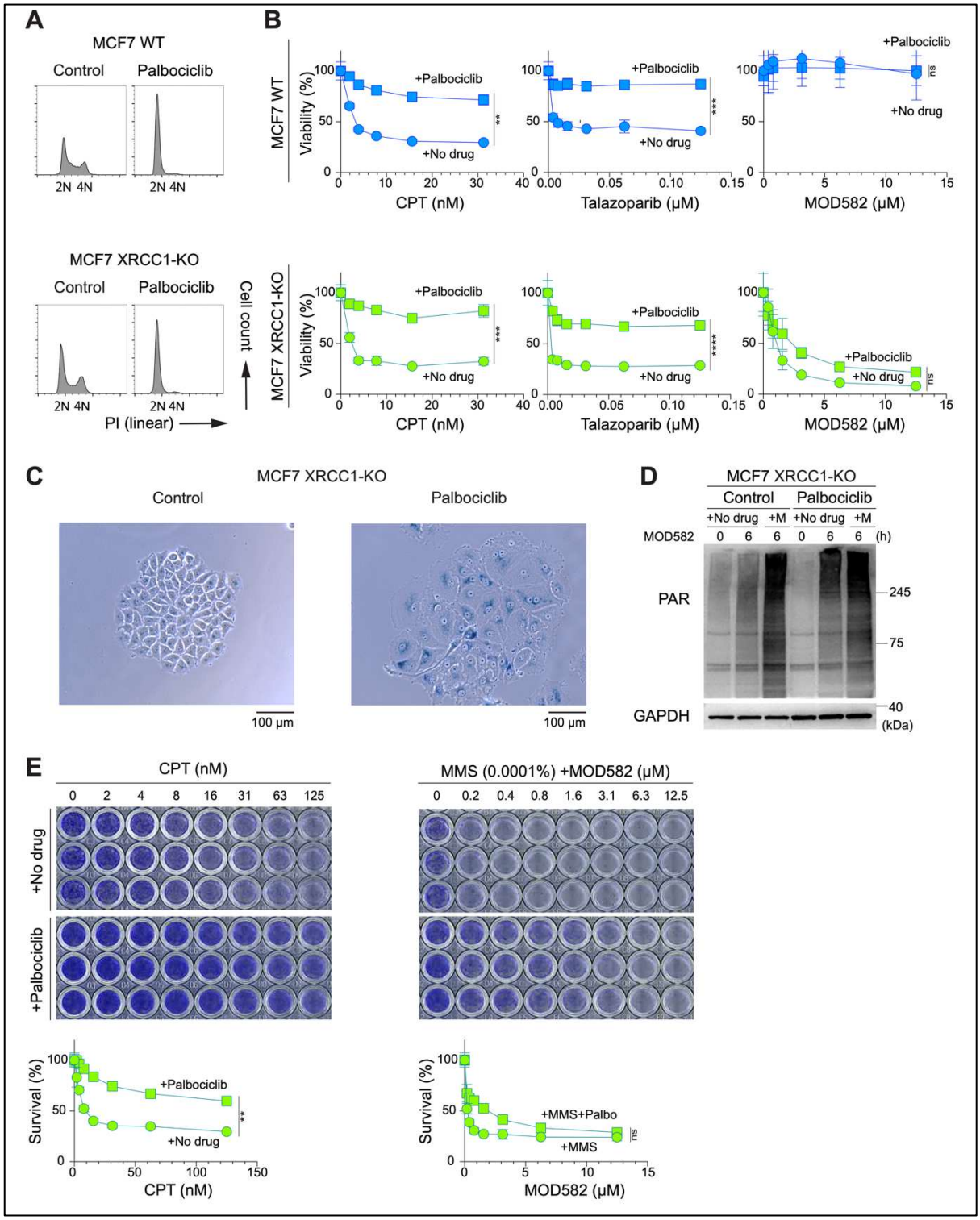


Figure 6. MOD582 effectively eliminates XRCC1-deficient cancer cells in G1 arrest and senescence-like states.

A Cell-cycle profiles of MCF7 WT and XRCC1-KO cells treated with the CDK4/6 inhibitor palbociclib (1000 nM) for 24 h. Cells were analyzed by propidium iodide staining followed by flow cytometry. **B** Viability of MCF7 WT (top) and XRCC1-KO (bottom) cells that were either untreated or pretreated with palbociclib (1000 nM) for 24 h, followed by treatment with CPT or talazoparib for 120 h, or MOD582 for 72 h, with or without palbociclib. Cell viability was normalized to untreated controls. Data represent mean ± SD (n=3, technical replicates) and represent one of three biologically independent experiments. $^{**}P < 0.01$; $^{***}P < 0.001$; $^{****}P < 0.0001$. ns, not significant. **C** Representative bright-field images of senescence-associated β-galactosidase (SA-β-gal) staining in MCF7 XRCC1-KO cells either untreated or treated with palbociclib (1000 nM) for 72 h. Scale bar, 100 µm. **D** Accumulation of PARylated proteins in MCF7 XRCC1-KO cells. Cells were either untreated or pretreated with palbociclib (1000 nM) for 72 h, followed by treatment with MOD582 (10 µM) with or without MMS. +M indicates MMS (0.0001%) treatment. Data represent one of two biologically independent experiments. **E** Clonogenic assays were performed in MCF7 XRCC1-KO cells either untreated or pretreated with palbociclib (1000 nM) for 72 h, followed by treatment with CPT or MOD582 in combination with MMS (0.0001%), where palbociclib treated cells were continuously treated with palbociclib. After 72 h of drug treatments, cells were stained with crystal violet (top) and quantified by acetic acid extraction to assess cell viability (bottom). Cell viability was normalized to untreated controls. Data represent mean ± SD (n=3, technical replicates) and represent one of three biologically independent experiments. $^{**}P < 0.01$. ns, not significant.

Discussion

Using the newly developed PARG inhibitors MOD568 and MOD582, we show that PARG inhibition induces cytotoxic accumulation of PARylated proteins and kills cancer cells, most effectively in BER-deficient contexts. Our findings indicate that this mechanism is not primarily driven by depletion of intracellular NAD^+ (Fig. 3) and is not adequately explained by canonical replication stress (Fig. 4). Instead, the data support a model in which sustained accumulation of PAR beyond a critical threshold is associated with a replication-independent death program featuring mitochondrial dysfunction and AIF translocation to the nucleus. This distinguishes PARG inhibition from replication-dependent cytotoxicity such as that induced by PARP inhibitors or topoisomerase I poisons. Importantly, this mechanism extends to G1-arrested and, in combination with low-dose MMS, enables efficient elimination of senescence-like cells, identifying a therapeutically relevant vulnerability in non-proliferating tumor cell states.

Our results suggest that cells can tolerate only a limited range of PARylation and identify BER deficiency as a strong sensitizing context for sensitivity to PARG inhibition, which activates PARP and induces hyperPARylation. However, clinical application remains challenging because core BER genes (e.g., XRCC1, POLB, and LIG1) are not commonly included in clinical gene panels, and reliable bioassays for BER deficiency have yet to be established. At the same

time, elevated PARP activity may result not only from BER defects but also from increased base damage under oxidative stress. Tumor cells frequently experience elevated reactive oxygen species due to metabolic reprogramming or hypoxia, especially in *in vivo* conditions, which may overwhelm BER capacity and create a state functionally analogous to BER deficiency (36). Consistent with this model, BER-proficient LoVo and A549 cells were relatively resistant to MOD568 *in vitro* but exhibited increased sensitivity in xenograft models, raising the possibility that the tumor microenvironment may enhance endogenous DNA damage and thereby promote toxic PAR accumulation upon PARG inhibition (Fig. 1). These observations support the concept that PARG inhibitor sensitivity may be driven by functional DNA damage load rather than strictly defined genetic defects. In this context, combining PARG inhibitors with agents that increase base damage, such as alkylating agents or ionizing radiation, may further enhance cytotoxicity and expand the therapeutic scope of PARG inhibition.

Our data further suggest that mitochondrial dysfunction contributes to PARG inhibitor–induced cytotoxicity (Fig. 5), although the underlying mechanism remains unclear. Several studies have shown that mitochondrial proteins can undergo PARylation, and that PARP1 or mitochondrial PARP (mtPARP) can localize to mitochondria under certain conditions (37, 38), raising the possibility that excessive PARylation disrupts mitochondrial homeostasis. Although our data demonstrate features consistent with parthanatos-like signaling, the presence of cleaved PARP1 indicates that apoptotic pathways may also be engaged. Together, these findings suggest that multiple mechanisms contribute to the cellular response to PARG inhibition in a context-dependent manner. Identifying cellular conditions that confer hypersensitivity to PARG inhibition beyond BER deficiency will be an important focus of future studies.

A particularly notable finding is that PARG inhibition retains cytotoxicity in G1-arrested and senescence-like cancer cells. Because many conventional anticancer therapies preferentially target proliferating cells, non-dividing or senescent tumor cells can persist and contribute to disease relapse. In contrast, our results demonstrate that PARG inhibition induces cytotoxicity independently of active DNA replication, thereby providing a strategy to target tumor cell populations that are relatively refractory to standard treatments. This feature may be particularly relevant in the context of therapy-induced senescence and residual disease.

Several limitations should be noted. First, our data do not exclude the possibility that replication stress contributes to PARG inhibitor sensitivity in other genetic or pharmacologic settings. Second, the most appropriate biomarkers for clinical stratification remain to be established. Third, although our findings support parthanatos-like signaling, they do not define a single linear execution pathway. Finally, the therapeutic window of PARG inhibition, particularly in combination with DNA-damaging agents, will require careful evaluation in normal tissues.

Together, our findings support a model in which excessive PAR accumulation represents a therapeutically exploitable vulnerability in cancer and establish PARG inhibition as a strategy for targeting both BER-deficient and non-proliferating tumor cell populations. These results provide a rationale for biomarker-driven patient stratification and combination strategies that enhance PAR accumulation to improve therapeutic efficacy.

Author contributions

Conceptualization: M.M., Y.T., J.M.

Methodology: E.K., M.M., T.U., T.S., T.T., Y.T., J.M.

Investigation: E.K., T.T., Y.T., R.K., S.T., S.N., S.K., J.M.

Formal analysis: E.K., M.M., T.U., T.S., T.T., Y.T., J.M.

Resources: H.S., K.H.

Writing – original draft: E.K., M.M., Y.T., J.M.

Supervision: Y.K., Y.U., Y.T., J.M.

Funding acquisition: Y.T., J.M.

Acknowledgement

We thank Ms. Mami Chosei and Mr. Mikio Nakane for technical assistance; Anil Srivastava, Srividya Swaminathan, Srinivasan Swaminathan, and Vinod Nayak Uppinangadi at Jubilant

Biosys Limited for coordination of the experimental activities and providing technical support; Sai Life Sciences, Inc. for performing the siRNA screening. We also acknowledge the support of ADRES (Advanced Research Support Center, Ehime University).

Financial support

This work was supported in part by the Japan Society for the Promotion of Science, Grants-in-Aid for Scientific Research (JP23H02768 to J.M.) and by the Japan Science and Technology Agency (JST) grant number JPMJFR2056 (JST FOREST Program to J.M).

References

1. Lord CJ, Ashworth A. (2012) The DNA damage response and cancer therapy. Nature 481:287-294.
2. Alemasova EE, Lavrik OI. (2019) Poly(ADP-ribosyl)ation by PARP1: reaction mechanism and regulatory proteins. Nucleic Acids Res 47:3811-3827.
3. Vyas S, Chang P. (2014) New PARP targets for cancer therapy. Nat Rev Cancer 14:502-509.
4. Murai J, Pommier Y. (2019) PARP Trapping Beyond Homologous Recombination and Platinum Sensitivity in Cancers. Annu Rev Canc Biol 3:131-150.
5. Murai J, Huang SY, Das BB, et al. (2012) Trapping of PARP1 and PARP2 by Clinical PARP Inhibitors. Cancer Res 72:5588-5599.
6. Murai J, Huang SY, Renaud A, et al. (2014) Stereospecific PARP trapping by BMN 673 and comparison with olaparib and rucaparib. Mol Cancer Ther 13:433-443.
7. Onji H, Murai J. (2022) Reconsidering the mechanisms of action of PARP inhibitors based on clinical outcomes. Cancer Sci 113:2943-2951.
8. Slade D. (2020) PARP and PARG inhibitors in cancer treatment. Genes Dev 34:360-394.
9. Zhou Y, Liu L, Tao S, et al. (2021) Parthanatos and its associated components: Promising therapeutic targets for cancer. Pharmacol Res 163:105299.
10. David KK, Andrabi SA, Dawson TM, Dawson VL. (2009) Parthanatos, a messenger of death. Front Biosci (Landmark Ed) 14:1116-1128.
11. Yu SW, Wang H, Poitras MF, et al. (2002) Mediation of poly(ADP-ribose) polymerase-1-dependent cell death by apoptosis-inducing factor. Science 297:259-263.
12. Moura RD, Mattos PD, Valente PF, Hoch NC. (2024) Molecular mechanisms of cell death by parthanatos: More questions than answers. Genet Mol Biol 47Suppl 1:e20230357.
13. Ravindranathan R, Somuncu O, da Costa A, et al. (2024) PARG inhibitor sensitivity correlates with accumulation of single-stranded DNA gaps in preclinical models of ovarian cancer. Proc Natl Acad Sci U S A 121:e2413954121.
14. Pillay N, Tighe A, Nelson L, et al. (2019) DNA Replication Vulnerabilities Render Ovarian Cancer Cells Sensitive to Poly(ADP-Ribose) Glycohydrolase Inhibitors. Cancer Cell 35:519-533 e518.

15. Coulson-Gilmer C, Morgan RD, Nelson L, et al. (2021) Replication catastrophe is responsible for intrinsic PAR glycohydrolase inhibitor-sensitivity in patient-derived ovarian cancer models. J Exp Clin Cancer Res 40:323.
16. Houl JH, Ye Z, Brosey CA, et al. (2019) Selective small molecule PARG inhibitor causes replication fork stalling and cancer cell death. Nat Commun 10:5654.
17. Saleh T, Bloukh S, Carpenter VJ, et al. (2020) Therapy-Induced Senescence: An "Old" Friend Becomes the Enemy. Cancers (Basel) 12.
18. Hernandez-Segura A, Nehme J, Demaria M. (2018) Hallmarks of Cellular Senescence. Trends Cell Biol 28:436-453.
19. Takahashi T, Shimizu T, Terada Y, Urakami T, Sinko W. (2024) Tetrahydrothienopyrimidinesulfonamide compounds. US.
20. Tucker JA, Bennett N, Brassington C, et al. (2012) Structures of the human poly (ADP-ribose) glycohydrolase catalytic domain confirm catalytic mechanism and explain inhibition by ADP-HPD derivatives. PLoS One 7:e50889.
21. Tomita A, Sasanuma H, Owa T, et al. (2023) Inducing multiple nicks promotes interhomolog homologous recombination to correct heterozygous mutations in somatic cells. Nat Commun 14:5607.
22. Leys C, Ley C, Klein O, Bernard P, Licata L. (2013) Detecting outliers: Do not use standard deviation around the mean, use absolute deviation around the median. Journal of Experimental Social Psychology 49:764-766.
23. James DI, Smith KM, Jordan AM, et al. (2016) First-in-Class Chemical Probes against Poly(ADP-ribose) Glycohydrolase (PARG) Inhibit DNA Repair with Differential Pharmacology to Olaparib. ACS Chem Biol 11:3179-3190.
24. Waszkowycz B, Smith KM, McGonagle AE, et al. (2018) Cell-Active Small Molecule Inhibitors of the DNA-Damage Repair Enzyme Poly(ADP-ribose) Glycohydrolase (PARG): Discovery and Optimization of Orally Bioavailable Quinazolinedione Sulfonamides. J Med Chem 61:10767-10792.
25. Erdelyi K, Bai P, Kovacs I, et al. (2009) Dual role of poly(ADP-ribose) glycohydrolase in the regulation of cell death in oxidatively stressed A549 cells. FASEB J 23:3553-3563.
26. Pan J, Fauzee NJ, Wang YL, et al. (2012) Effect of silencing PARG in human colon carcinoma LoVo cells on the ability of HUVEC migration and proliferation. Cancer Gene Ther 19:715-722.
27. Mortusewicz O, Haslam J, Gad H, Helleday T. (2025) Uracil-induced replication stress drives mutations, genome instability, anti-cancer treatment efficacy, and resistance. Mol Cell 85:1897-1906.
28. Sasanuma H, Tsuda M, Morimoto S, et al. (2018) BRCA1 ensures genome integrity by eliminating estrogen-induced pathological topoisomerase II-DNA complexes. Proc Natl Acad Sci U S A 115:E10642-E10651.
29. Ibrahim MA, Yasui M, Saha LK, Sasanuma H, Honma M, Takeda S. (2020) Enhancing the sensitivity of the thymidine kinase assay by using DNA repair-deficient human TK6 cells. Environ Mol Mutagen 61:602-610.
30. Pommier Y. (2006) Topoisomerase I inhibitors: camptothecins and beyond. Nat Rev Cancer 6:789-802.
31. Murai J, Thomas A, Miettinen M, Pommier Y. (2019) Schlafen 11 (SLFN11), a restriction factor for replicative stress induced by DNA-targeting anti-cancer therapies. Pharmacol Ther 201:94-102.
32. Ogawa A, Izumikawa K, Tate S, et al. (2025) SLFN11-mediated ribosome biogenesis impairment induces TP53-independent apoptosis. Mol Cell 85:894-912 e810.

33. Fujiwara K, Maekawa M, Iimori Y, et al. (2023) The crucial role of single-stranded DNA binding in enhancing sensitivity to DNA-damaging agents for Schlafen 11 and Schlafen 13. iScience 26:108529.
34. Murai J, Tang SW, Leo E, et al. (2018) SLFN11 Blocks Stressed Replication Forks Independently of ATR. Mol Cell 69:371-384 e376.
35. Onji H, Tate S, Sakaue T, et al. (2024) Schlafen 11 further sensitizes BRCA-deficient cells to PARP inhibitors through single-strand DNA gap accumulation behind replication forks. Oncogene 43:2475-2489.
36. Weinberg F, Ramnath N, Nagrath D. (2019) Reactive Oxygen Species in the Tumor Microenvironment: An Overview. Cancers (Basel) 11.
37. Lee JH, Hussain M, Kim EW, et al. (2022) Mitochondrial PARP1 regulates NAD(+)-dependent poly ADP-ribosylation of mitochondrial nucleoids. Exp Mol Med 54:2135-2147.
38. Szczesny B, Brunyanszki A, Olah G, Mitra S, Szabo C. (2014) Opposing roles of mitochondrial and nuclear PARP1 in the regulation of mitochondrial and nuclear DNA integrity: implications for the regulation of mitochondrial function. Nucleic Acids Res 42:13161-13173.

Supplementary Files

This is a list of supplementary files associated with this preprint. Click to download.

- TableS1datacollectionrefinementstatisticsfinal.pdf
- TableS2SupplementaldatasiRNA.xlsx
- ApoptosisSupplementalinformation.pdf